

Absolute Nodal Coordinates in Digital Image Correlation

Cite as:

M. Langerholc, J. Slavič and M. Boltežar: Absolute Nodal Coordinates in Digital Image Correlation. Experimental Mechanics, Vol. 53 (5), p. 807-818, 2013.

Marko Langerholc^{a,b}, Janko Slavič^a, Miha Boltežar^a

^aUniversity of Ljubljana, Faculty of Mechanical Engineering, Aškerčeva 6, 1000 Ljubljana, SI, Slovenia

^bKnauf Insulation d.o.o., Trata 32, 4220 Škofja Loka, SI, Slovenia

Abstract

A great deal of progress has been made in recent years in the field of global digital image correlation (DIC), where higher-order, element-based approaches were proposed to improve the interpolation performance and to better capture the displacement fields. In this research, another higher-order, element-based DIC procedure is introduced. Instead of the displacements, the elements' global nodal positions and nodal position-vector gradients, defined according to the absolute nodal coordinate formulation, are used as the searched parameters of the Newton–Raphson iterative procedure. For the finite elements, the planar isoparametric plates with 24 nodal degrees of freedom are employed to ensure the gradients' continuity among the elements. As such, the presented procedure imposes no linearization on the strain measure, and therefore indicates a natural consistency with the nonlinear continuum theory. To verify the new procedure and to show its advantages, a real large deformation experiment and several numerical tests on the computer-generated images are studied for the standard, low-order, element-based digital image correlation and the presented procedure. The results show that the proposed procedure proves to be accurate and reliable for describing the rigid-body movement and simple deformations, as well as for determining the continuous finite strain field of a real specimen.

1. Introduction

In recent years, digital image correlation (DIC) has become a well-established optical method for determining displacement and deformation fields by relating the grayscale intensity values of surface images before and after deformation. As an experimental procedure, DIC has been extensively used in a variety of applications, e.g., it is frequently employed for the characterization of complex materials [25, 27, 21] and deformation or damage mechanisms [11, 13]. There are many advantages of the DIC, among others a relatively low-cost experimental equipment, simple and fast specimen preparation and no limitations to specimen deformation (as long as the specimen stays in the camera frame) [12]. Additionally, the experiments are not restricted to laboratory environment and are therefore suitable for on-site measurements.

In the DIC procedure, two main approaches were established to relate the reference and the deformed image, i.e., the pointwise and the global approach. The pointwise approach [12] is frequently used due to its simplicity and speed, despite the drawbacks of occasionally incorrectly identified displacement data and the need for additional displacement-field smoothing. The global approach was introduced to resolve some of these problems by analyzing the entire region of interest (ROI) at once [5]. Sun *et al.* [20] managed to implement the finite-element framework into the global approach, where the ROI was divided into inter-connected finite elements. Besnard *et al.* [2] further developed the method based on the optical flow, and employed the most commonly used bilinear shape functions for 4-noded plate elements to define the displacement fields (Q4-DIC).

By using the finite-element framework, the displacement continuity requirements were naturally satisfied and the deformation field was obtained without the need for additional smoothing. For this reasons the global approach, based on the element discretization of the ROI (*element-based DIC* or *FE-DIC*), is gaining in popularity and has already been successfully used in many different applications, e.g., [8, 21]. In most cases, the Q4-DIC is employed, which uses the low-order elements that use the displacements for nodal degrees of freedom (DOF), only - a drawback that directly affects the identified displacement and strain fields. To address the problems regarding the low-order interpolation, higher-order elements were introduced into the DIC. Ma *et al.* [30] proposed Q8-DIC, i.e., the implementation of 8-noded elements using third-order shape functions to better cover the specimen with curve edges and to describe more complex deformation fields. Further, by using the experiment-relevant higher-order shape functions, Hild *et al.* [31] proposed a *Beam-DIC* as an integrated approach to directly identify the Euler-Bernoulli beam global DOFs, without the need for post-processing the measured displacements. Last, to improve the DIC performance in terms of lower uncertainty and noise levels for both the displacements and strains, Réthoré *et al.* [14] implemented higher-order NURBS functions; their formulation of the DIC also gave better results than the higher-order C_0 continuous plate elements.

By using these approaches, the strain field could be better captured and fewer and bigger elements could be employed due to the higher performance of the elements. However, the use of these formulations for large-deformation cases was not explicitly addressed in these investigations. There are special procedures to be used for large-deformation analysis, as shown by Hild *et al.* in [32]. Furthermore, the drawback of the use of displacements to analyze highly nonlinear systems still exists, since it is generally preferable to restrict the use of the displacements to linear strain analysis and define the nonlinear strain measures based on the global point positions [4].

In this research, another global, FE-DIC procedure is presented that introduces a new interpolation scheme. Instead of the displacements, both the global nodal positions and the nodal position-vector gradients of the isoparametric finite elements are defined as searched parameters that are directly identified from the image-correlation process. For these reasons the presented procedure indicates a natural consistency with the continuum theory and therefore makes it possible to directly implement nonlinear strain measures. Due to the global element representation, a relation between the DIC and the special large-deformation finite-element method, the absolute nodal coordinate formulation (ANCF), is established.

The ANCF was presented by Shabana to analyze the dynamics of flexible bodies undergoing finite rotation and deformation [17, 16]. In the ANCF, the position of the material point is described in the global coordinate system according to the continuum theory, with the use of the nonlinear Green-Lagrange strain tensor as a deformation measure. For the finite element, the global position coordinates and position-vector gradients are defined as the nodal coordinates, and there is no limitations on the amount of deformation and rotation of the element. Due to its

numerous advantages, the ANCF has been successfully employed in many different applications, e.g., [19, 26, 7, 22, 23]. Although the ANCF is primarily developed to analyze dynamical systems, its advantages are now also exploited in the field of DIC.

Since in DIC we are dealing with a two-dimensional planar continuum, the use of reduced-order ANCF plate elements is implied [6, 15, 18]. These plates satisfy the nodal positions and nodal position-vector gradients continuity among the elements, as well as the displacement continuity along their boundaries. Each of the elements has 4 nodes with 6 nodal coordinates. These coordinates, which are directly obtained from the correlation process, are further used to define the nonlinear in-plane Green–Lagrange strain field. The presented procedure, called the *ANCF–DIC*, therefore extends the Q4–DIC in taking advantage of the ANCF in terms of the nonlinear continuum theory. As such, the ANCF–DIC presents an alternative experimental-numerical analysis of dynamical systems, e.g. [10], or to the constitutive parameters identification, where the consideration of finite strains is necessary [1].

To verify the new procedure and to show its advantages, numerical simulations of simple deformations, rigid-body translation and rotation are studied first on computer-generated images (CGI) and compared with the Q4–DIC. These simulations are made for several element sizes and deformation conditions. A real large-deformation experiment is then executed and analyzed using both methods to observe the strain fields and the displacement field continuity.

The paper is organized as follows: In Section 2, a short description of the ANCF theory in relation to the plate element is given. The Q4–DIC is also presented in Section 2 as the basis for the further development of the method, followed by the introduction of the ANCF–DIC procedure. In Section 3, the numerical simulations and the experiment, together with the results, are presented. The conclusions follow in Section 4.

2. Theoretical background

2.1. Reduced-order ANCF plate element

In the absolute nodal coordinate formulation, the plate elements were developed to overcome some of the degenerate FE plates’ drawbacks [19]. The elements of different orders with respect to the number of the nodal DOF were proposed to capture the desired deformation modes [6]. Since only the plane deformation is analyzed in the DIC, the reduced-order plate element is employed without any consideration of the thickness direction.

The global position-vector \mathbf{r}_j of the point on the j -th plate element (Fig. 1) is defined in the plane as

$$\mathbf{r}_j(\mathbf{x}_j) = [r_{1j} \ r_{2j}]^T = \mathbf{S}_j(\mathbf{x}_j) \mathbf{e}_j, \quad (1)$$

where $\mathbf{x}_j = [x_{1j}, \ x_{2j}]^T$ is the local point position, \mathbf{e}_j is the vector of the element’s nodal coordinates

$$\mathbf{e}_j = [\mathbf{e}_j^{1T} \ \mathbf{e}_j^{2T} \ \mathbf{e}_j^{3T} \ \mathbf{e}_j^{4T}]^T, \quad (2)$$

where the global nodal positions and position-vector gradients are

$$\mathbf{e}_j^k = [\mathbf{r}_j^k \ \mathbf{r}_{j,x_{1j}}^k \ \mathbf{r}_{j,x_{2j}}^k]^T, \quad k = 1, 2, 3, 4, \quad (3)$$

where

$$\mathbf{r}_{j,x_{lj}}^k = \frac{\partial \mathbf{r}_j^k}{\partial x_{lj}}, \quad (4)$$

and $\mathbf{S}_j(\mathbf{x}_j)$ is the matrix of the element shape functions [7] (see Appendix for details). The reduced-order plate possesses 24 nodal DOF altogether, which completely describe the element's configuration with 12 bicubic shape functions of the matrix \mathbf{S} .

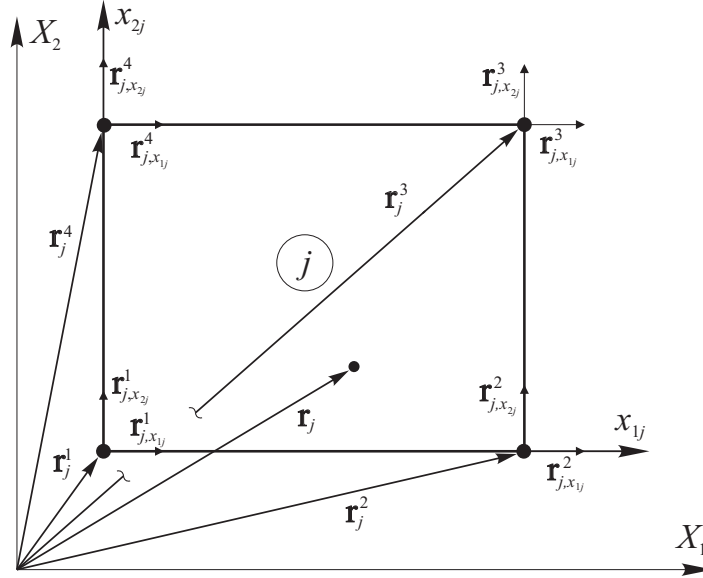


Figure 1: Planar ANCF plate element; global nodal positions and nodal position-vector gradients

In the ANCF, the rotation angle θ may be obtained from the orthogonal rotation matrix [4]

$$\mathbf{R} = \begin{bmatrix} \cos \theta & -\sin \theta \\ \sin \theta & \cos \theta \end{bmatrix}, \quad (5)$$

which is defined with the polar decomposition of the position-vector gradients matrix \mathbf{J}

$$\mathbf{J} = \mathbf{R}\mathbf{U}, \quad (6)$$

where \mathbf{U} is the stretch tensor and

$$\mathbf{J} = \frac{\partial r_i}{\partial x_k}, \quad i, k = 1, 2. \quad (7)$$

For the deformation measure, the globally defined, nonlinear, in-plane Green-Lagrange strain tensor is used

$$\boldsymbol{\varepsilon} = \frac{1}{2} [\mathbf{J}^T \mathbf{J} - \mathbf{I}], \quad (8)$$

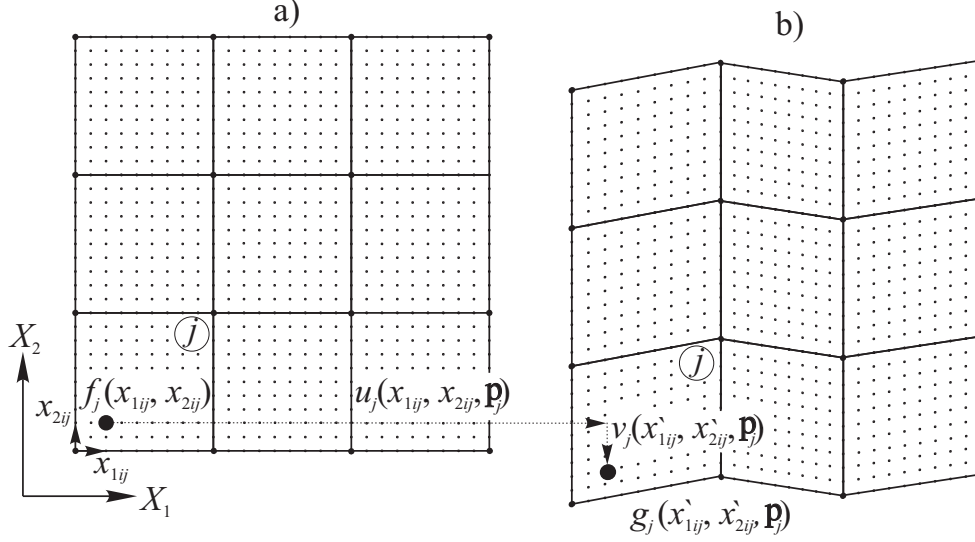


Figure 2: Main features of the Q4-DIC procedure, using the bilinear shape functions; a) The reference image, b) The deformed image

where \mathbf{I} is a 2×2 identity matrix. Considering the relations (1), (7) and (8), the in-plane Green-Lagrange strain tensor of the j -th element is defined in terms of its nodal coordinates as

$$(\varepsilon_{kl})_j = \frac{1}{2} \left(\mathbf{e}_j^T \left(\frac{\partial \mathbf{S}_j}{\partial x_{kj}} \right)^T \frac{\partial \mathbf{S}_j}{\partial x_{lj}} \mathbf{e}_j - \delta_{kl} \right), \quad k, l = 1, 2. \quad (9)$$

It is the absolute nodal coordinate formulation, summarized in this subsection, that is used to extend the Q4-DIC. Since the latter presents the basis for the further development of the method, it is summarized first.

2.2. The Q4-DIC

Q4-DIC has been well researched in terms of its accuracy, robustness and reliability [20, 2]. The correlation procedure between the reference image (Fig. 2-a) and the deformed image (Fig. 2-b) starts here by dividing the region of interest (ROI) into elements, which are connected at the common nodes [20]. Between the elements, only the displacement continuity is usually required. In contrast to the subset-based DIC, the correlation procedure is executed over all the nodal displacements at once.

Let (x_{1ij}, x_{2ij}) and (x'_{1ij}, x'_{2ij}) be the i -th point in the j -th element of the reference and the deformed image, respectively. In the Q4-DIC, the least-squares correlation coefficient is defined for the grayscale intensity levels $f_j(x_{1ij}, x_{2ij})$ and $g_j(x'_{1ij}, x'_{2ij})$ for all the elements at once

$$C = \frac{\sum_{j=1}^n \sum_{i=1}^M (f_j(x_{1ij}, x_{2ij}) - g_j(x'_{1ij}, x'_{2ij}, \mathbf{P}_j))^2}{\sum_{j=1}^n \sum_{i=1}^M f^2(x_{1ij}, x_{2ij})}, \quad (10)$$

where n is the number of elements and M is the number of the element's points. The point location in the deformed element is defined as

$$x'_{1ij} = x_{1ij} + u_j(x_{1ij}, x_{2ij}, \mathbf{p}_j), \quad (11)$$

$$x'_{2ij} = x_{2ij} + v_j(x_{1ij}, x_{2ij}, \mathbf{p}_j), \quad (12)$$

where \mathbf{p}_j is the vector of the element's displacements

$$\mathbf{p}_j = [u_{1j}, v_{1j}, \dots, u_{mj}, v_{mj}]^T, \quad (13)$$

and m is the number of element nodes. In contrast to the subset-based DIC, the displacement fields are defined as

$$u_j(x_{1ij}, x_{2ij}, \mathbf{p}_j) = \sum_{k=1}^m A_k(\xi, \eta) u_{kj}, \quad (14)$$

$$v_j(x_{1ij}, x_{2ij}, \mathbf{p}_j) = \sum_{k=1}^m A_k(\xi, \eta) v_{kj}, \quad (15)$$

where $A_k(\xi, \eta)$ are, in this case, the most commonly used bilinear shape functions of the conventional rectangular plate element [29]. The minimization of the correlation coefficient (10) is executed over all the ROI using the Newton–Raphson procedure

$$\nabla \nabla C(\mathbf{p}_0) (\mathbf{p} - \mathbf{p}_0) = -\nabla C(\mathbf{p}_0), \quad (16)$$

to obtain the displacement parameter vector \mathbf{p} of all the elements

$$\mathbf{p} = [u_1, v_1, \dots, u_N, v_N]^T, \quad (17)$$

where N is the total number of nodes and \mathbf{p}_0 is the initial approximation.

To execute the Newton–Raphson procedure (16), the derivatives of the grayscale intensity of the deformed image g with respect to the parameter vector (17) components are required. These can be obtained from the most frequently employed bicubic sub-pixel interpolation [3]

$$g(x'_1, x'_2) = \sum_{r=0}^3 \sum_{s=0}^3 \alpha_{rs} (x'_1)^r (x'_2)^s, \quad (18)$$

where α_{rs} are the coefficients of the bicubic surface, obtained with the grayscale intensity level of the neighbouring points and the continuity requirements.

The unknown parameter vector (17) consists of $2N$ components, which represent the displacements of all the nodes. The displacement field is defined by the shape functions, from which the Green–Lagrange strain components

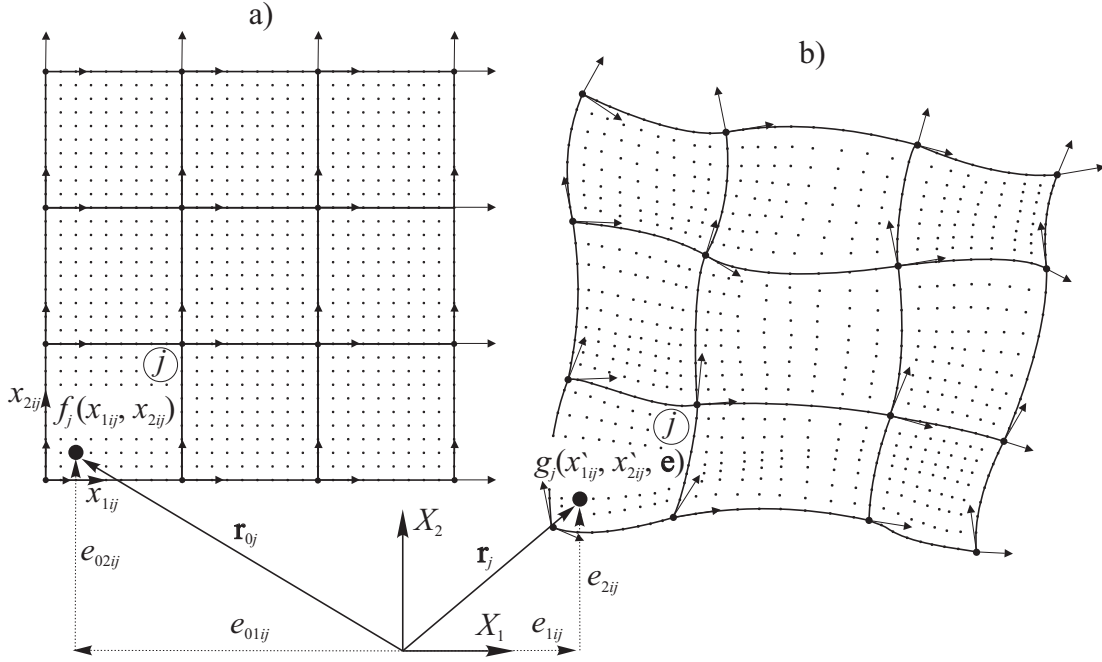


Figure 3: Main features of the ANCF-DIC; a) The reference image, b) The deformed image

are defined as

$$\varepsilon_{11} = \frac{\partial u}{\partial x_1} + \frac{1}{2} \left[\left(\frac{\partial u}{\partial x_1} \right)^2 + \left(\frac{\partial v}{\partial x_1} \right)^2 \right], \quad (19)$$

$$\varepsilon_{22} = \frac{\partial v}{\partial x_2} + \frac{1}{2} \left[\left(\frac{\partial v}{\partial x_2} \right)^2 + \left(\frac{\partial u}{\partial x_2} \right)^2 \right], \quad (20)$$

$$\varepsilon_{12} = \frac{1}{2} \left(\frac{\partial u}{\partial x_2} + \frac{\partial v}{\partial x_1} + \frac{\partial u}{\partial x_1} \frac{\partial u}{\partial x_2} + \frac{\partial v}{\partial x_1} \frac{\partial v}{\partial x_2} \right), \quad (21)$$

and in the case of small rigid-body rotations, the approximate angle of rotation is determined as [20]

$$\theta \approx \frac{1}{2} \left(\frac{\partial v}{\partial x_1} - \frac{\partial u}{\partial x_2} \right). \quad (22)$$

2.3. Absolute nodal coordinates in DIC

The ANCF-DIC is introduced here for the first time (Fig. 3). The procedure follows the steps of Section 2.2 with the implementation of the absolute nodal coordinates, where the main difference lies in the continuum approach and an additional consideration of the nodal position-vector gradients.

The correlation criterion (10) is rewritten as

$$C = \frac{\sum_{j=1}^n \sum_{i=1}^M (f_j(x_{1ij}, x_{2ij}) - g_j(x'_{1ij}, x'_{2ij}, \mathbf{e}_j))^2}{\sum_{j=1}^n \sum_{i=1}^M f^2(x_{1ij}, x_{2ij})}, \quad (23)$$

where \mathbf{e}_j is the element parameter vector, which consists of the reduced-order ANCF plate element nodal coordinates, i.e., the global nodal positions and the nodal position-vector gradients (2, 3)

$$\mathbf{e}_j = [e_{11j}, \dots, e_{61j}, \dots, e_{1mj}, \dots, e_{6mj}]^T, \quad (24)$$

where e_{kmj} is the k -th nodal coordinate of the j -th element's m -th node. In contrast to the Q4-DIC, the displacement of an arbitrary point δx_{kij} on the deformed element (14, 15) is defined globally

$$\delta x_{kij} = x'_{kij} - x_{0kij} = \mathbf{S}_{ij}(\mathbf{e}_j - \mathbf{e}_0) \parallel_k, \quad k = 1, 2, \quad (25)$$

where \parallel_k stands for the k -th direction and $\mathbf{S}_{ij} = \mathbf{S}_j(x_{1ij}, x_{2ij})$ are the values of the element's shape functions at the i -th point (see Appendix). By defining \mathbf{e}_0 and \mathbf{e} as the parameter vectors of all the elements' nodes of the reference and the deformed image, respectively

$$\mathbf{e} = [e_{111}, \dots, e_{611}, \dots, e_{1mn}, \dots, e_{6mn}]^T, \quad (26)$$

$$\mathbf{e}_0 = [e_{0111}, \dots, e_{0611}, \dots, e_{01mn}, \dots, e_{06mn}]^T, \quad (27)$$

where n is the total number of elements, the correlation coefficient (23) is minimized using the Newton-Raphson procedure

$$\nabla \nabla C(\mathbf{e}_0)(\mathbf{e} - \mathbf{e}_0) = -\nabla C(\mathbf{e}_0), \quad (28)$$

where

$$\nabla C = \left(\frac{\partial C}{\partial \mathbf{e}} \right) = -2D \sum_{j=1}^n \mathbf{E}_j^T \left\{ \sum_{i=1}^M (f_j(x_{1ij}, x_{2ij}) - g_j(x'_{1ij}, x'_{2ij}, \mathbf{e}_j)) \frac{\partial g_j(x'_{1ij}, x'_{2ij}, \mathbf{e}_j)}{\partial e_l} \right\}_{1, \dots, 6m}, \quad (29)$$

and D is a constant

$$D = \left(\sum_{j=1}^n \sum_{i=1}^M f^2(x_{1ij}, x_{2ij}) \right)^{-1}. \quad (30)$$

\mathbf{E}_j is the $6m \times 6n$ assembly matrix, which in contrast to the Q4-DIC, also connects the nodal position-vector gradients of the j -th element with the values of the other neighbouring elements. To see the construction of the assembly matrix, the interested reader is referred to [30].

Considering the Vendroux and Knauss [24] numerical improvement of the Hessian matrix calculation, the second derivatives of the correlation coefficient are written as

$$\nabla \nabla C = \left(\frac{\partial^2 C}{\partial \mathbf{e}^2} \right) = 2D \sum_{j=1}^n \mathbf{E}_j^T \left\{ \sum_{i=1}^M \frac{\partial g_j(x'_{1ij}, x'_{2ij}, \mathbf{e}_j)}{\partial e_k} \frac{\partial g_j(x'_{1ij}, x'_{2ij}, \mathbf{e}_j)}{\partial e_l} \right\}_{\substack{k=1, \dots, 6m \\ l=1, \dots, 6m}} \mathbf{E}_j \quad (31)$$

The Newton–Raphson procedure (28) converges on the norm of the parameter vector difference $\|\delta \mathbf{e}_i\| = \|\mathbf{e}_i - \mathbf{e}_{i-1}\|$, based on which the convergence criterion is established. The computation stops at the k -th iteration, when $\|\delta \mathbf{e}_k\| < \epsilon$, where ϵ is a prescribed value.

As before, the bicubic sub-pixel interpolation of the grayscale intensity is required to obtain the derivatives for (29) and (31). Using the relations (18) and (25), the grayscale intensity at an arbitrary point of the deformed element is defined as

$$g_j(x'_{1ij}, x'_{2ij}, \mathbf{e}) = \sum_{r=0}^3 \sum_{s=0}^3 \alpha_{rs} (\mathbf{S}_{ij} \mathbf{E}_j \mathbf{e} \|_1)^r (\mathbf{S}_{ij} \mathbf{E}_j \mathbf{e} \|_2)^s . \quad (32)$$

The derivatives are then obtained using the chain rule of differentiation

$$\frac{\partial g_j(x'_{1ij}, x'_{2ij}, \mathbf{e})}{\partial e_a} = \sum_{k=1}^2 \frac{\partial g_j(x'_{1ij}, x'_{2ij}, \mathbf{e})}{\partial x'_{kij}} \mathbf{S}_{ij} \frac{\partial (\mathbf{E}_j \mathbf{e})}{\partial e_a} \Big|_k . \quad (33)$$

From the obtained parameter vector (26), i.e., the global nodal positions and nodal position-vector gradients of all the nodes in the ROI, the new configurations of the finite elements in the deformed image are determined by

$$\mathbf{r}_j = \mathbf{S}_j \mathbf{E}_j \mathbf{e} , \quad (34)$$

from which the rotation field and the in-plane Green-Lagrange strain components are determined using (5)-(7) and (9), respectively. It is worth noting at this point that the number of parameters in the Newton–Raphson procedure for the ANCF–DIC is three times higher than that for the Q4–DIC due to the implementation of the nodal position-vector gradients. However, one could omit the number of nodal parameters and still keep the global description of the elements, like, e.g., in [28].

3. Numerical verification and real experiment

To verify the new method and to show its advantages, a comparison between the Q4–DIC and the ANCF–DIC procedures are made. For both procedures, the analyses are executed on both the computer-generated (CGI) and real images under the specific computer-imposed and real deformation conditions. For all the computer-generated deformation cases, the results are compared in terms of the obtained values' differences from the prescribed ones, and the standard deviations

$$\sigma_A = \left(\frac{1}{n_t - 1} \sum_{i=1}^{n_t} (x_i - \bar{x})^2 \right)^{1/2} , \quad (35)$$

where A is the analyzed variable and n_t is the total number of analyzed points.

For both methods, the setup and deformation conditions are identical. A square ROI is chosen and analyzed with the same number of 4-node square plate elements, and the elements' size and the pixel locations for the nodal position coordinates are also the same.

It is commonly known that in the global DIC approach, the boundary elements perform poorly due to the lack of continuity requirements [2]. For our purpose of assessing the ANCF–DIC with standard tests, the boundary elements are therefore excluded [20], and only the interior elements are considered for the interpretation of the results.

3.1. Numerical experiment

A numerical experiment is executed on a CGI, represented by a simple two-dimensional grayscale function $f(x_1, x_2) = 0.5(\sin(x_1)/10 + \cos(x_2)/10)$. The purpose of this study is to determine the ANCF–DIC performance without the influence of the instrumentation errors. The simulated simple deformation conditions, defined like in [20], consist of the numerically generated image stretch, rigid-body translation and rotation. These conditions are imposed on the images with a defined 421×421 and 401×401 pixels ROI. This area is analyzed using finite elements of different sizes: 30×30 , 40×40 and 50×50 pixels. The prescribed image-rotation angle is 1 degree (0.017453 rad), the strains are $\varepsilon_{011} = \varepsilon_{022} = 0.012$, and the vertical and horizontal displacements are 0.5 pixels. All the deformed images are generated using Matlab® [9].

The comparison of the results for the Q4–DIC and the ANCF–DIC is presented in Table 1. For all the deformation cases, the Q4–DIC describes the displacement data and the strain standard deviations better than the ANCF–DIC. This is generally the case when the higher-order approaches are used, since the number of unknowns for these approaches is larger. In comparison with the other higher-order approaches [30, 14], the ANCF–DIC gives roughly similar results; the standard deviations are by up to one order of magnitude higher than those of the Q4–DIC, for the same element size.

Both methods give better results, if the element’s size increases. When analyzing simple deformation cases, this suggests that fewer and bigger elements are used to achieve better accuracy. However, when analyzing complex (heterogeneous) deformations with the large Q4–DIC elements, the obtained results may not be accurate enough due to the bilinear interpolation. Further, if a finer discretization with the Q4 elements is employed, the performance of the elements starts to deteriorate [30] and the obtained stain fields are still discontinuous at the elements’ nodes.

3.2. Large-deformation experiment

To show the advantages of the ANCF–DIC over the Q4–DIC, a large deformation experiment was designed using a specimen of an uncrimped stonewool fleece [33] (Fig. 4). The material of the specimen is known to be a highly deformable, heterogeneous and anisotropic fiber-reinforced composite continuum, made of a mixture of stone fibres and binding resin. This material was chosen for analysis since it possesses a naturally speckled surface and offers great flexibility in obtaining large deformation states with relatively small forces.

There are special procedures to be used for the large-deformation analysis in the DIC, as shown by Hild *et al.* in [32]. In our case, the image-updating procedure is employed, i.e., for every next step, the deformed image of the previous step becomes the next reference image. The updating procedure has the drawback of error accumulation; however, Hild *et al.* [32] showed that the strategy is robust and allows the identification of strains of order 1 and higher.

A specimen of 401×401 pix size was chosen and discretized into 64 elements of 50×50 pix size (Fig. 6). The specimen was fixed into an experimental device, which consists of an automatic rotation stage with installed vertical needles, surrounded by a fixed framework (Fig. 5-a). The needles were fixed radially from the center to grab the specimen during the stage rotation, regulated by the stepper motor, controller and PC. During the experiment, a CMOS Casio EX-FH25 high-speed camera was used to record the deformation. The whole experimental setup is shown in Fig. 5-b. The specimen deformation was achieved with a stage rotation of 40° with a constant speed of $1^\circ/\text{s}$ (Fig. 6). For the analysis, 23 successive and equally time-spaced images were extracted from the recording

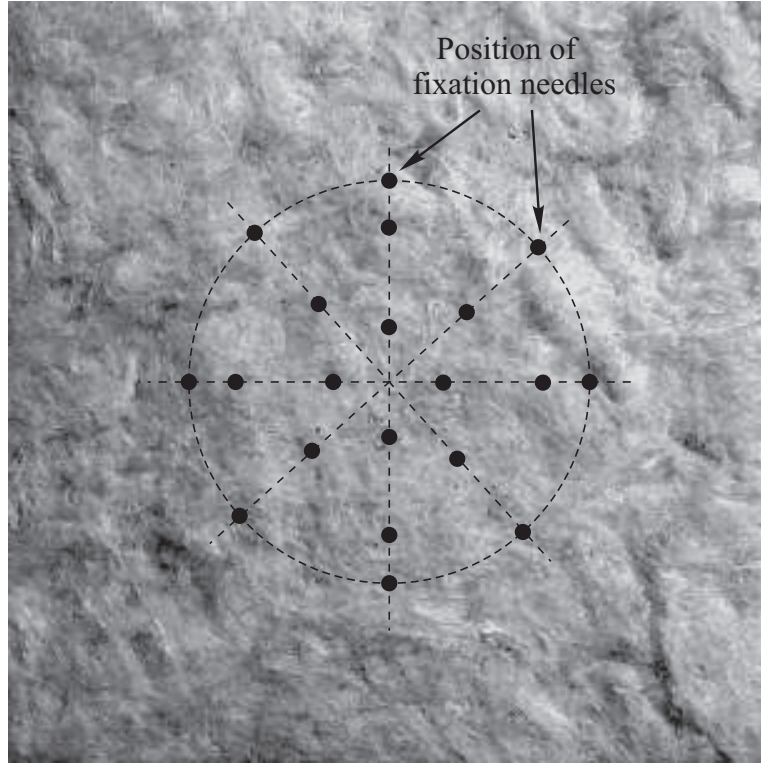


Figure 4: Uncrimped stone wool fleece specimen for the deformation experiment

and normalized to the grayscale interval. The use of 23 images for 40° rotation may, in our case, cause a maximum displacement of approximately 6 pixels between the two consecutive images. The convergence threshold for the NR algorithm was set to $\varepsilon = 5 \cdot 10^{-3}$. The results of the experiment are shown in Fig. 6. The displacement field of the Q4-DIC (Fig. 6-a) is continuous; however, the deformation of the elements is of low-order due to the bilinear shape functions. On the other hand, due to the full nodal parametrization of the elements, the displacement field of the ANCF-DIC (Fig. 6-b) satisfies the displacement continuity along the elements' boundaries, even though higher-order shape functions are used. These shape functions also allow the elements greater flexibility in adapting to the image grayscale changes, which indicates that a smaller number of elements may be used to achieve an adequate correlation performance. The only drawback of the ANCF-DIC is the computational cost; due to the increased number of nodal parameters the simulation time is approximately one order of magnitude higher than that for the Q4-DIC. Fig. 7 shows the strain fields of the last deformed image from the experiment. The Q4-DIC strain fields are discontinuous at the elements nodes and are uniform in the direction of the displacement field differentiation for the ε_{11} and ε_{22} strains. On the other hand, the ANCF-DIC captures the higher-order, in-plane Green-Lagrange strains in addition to the nodal strain continuity. To compare the amplitudes of the identified strains, the maximal strain values in the areas of the strain concentrations are analyzed for the Q4-DIC and the ANCF-DIC. In the present case, the maximal values

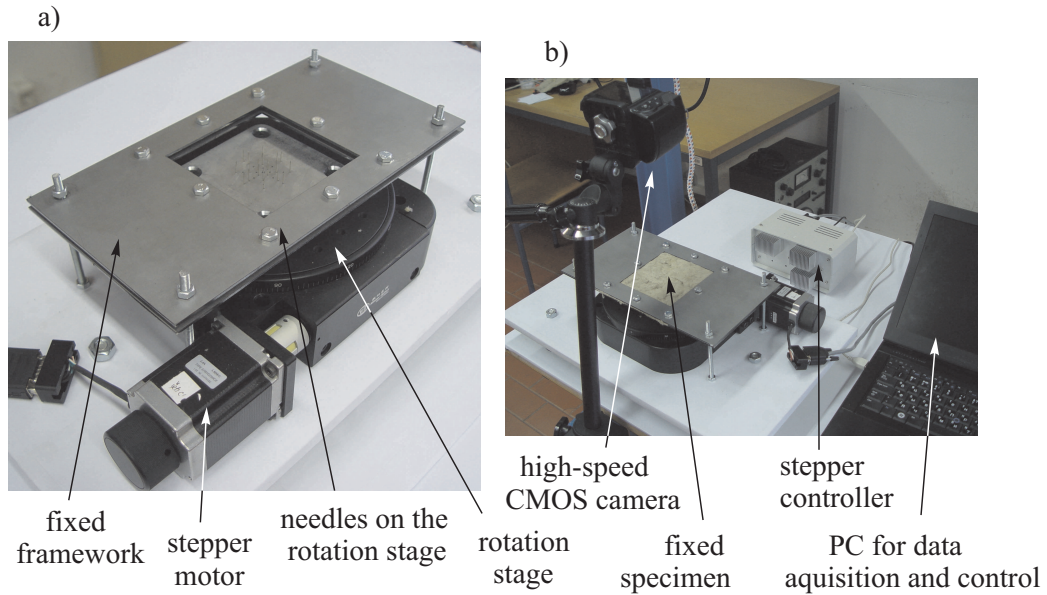


Figure 5: Large deformation experiment: a) The rotation stage with vertical needles, b) The experimental setup

of the Q4-DIC are by 103 %, 27 % and 60 % lower than that of the ANCF-DIC, for ε_{11} , ε_{22} and ε_{12} , respectively (Fig. 7). The considerable difference in maximal strain values is contributed to the higher-order interpolation and the increased number of the nodal DOF of the ANCF elements.

4. Conclusions

In this research, an alternative procedure in the global digital image correlation (DIC) is introduced. Basically a finite-element approach to the image correlation process (FE-DIC), the procedure implements the recently developed absolute nodal coordinate formulation (ANCF), which allows a specimen deformation analysis according to the nonlinear continuum theory. The ANCF-DIC procedure employs the nonlinear, in-plane Green-Lagrange strain tensor for the deformation measure that is defined with the nodal position-vector gradients of the planar ANCF plate elements. The verification and performance evaluation of the new procedure is performed with numerical tests on a computer-generated image (CGI) and a real large-deformation experiment. The research is summarized as follows:

1. By employing the ANCF plate elements, which also include the nodal position-vector gradients, the displacement continuity along the elements' boundaries is satisfied.
2. Due to the use of the higher-order shape functions, the globally defined nonlinear, in-plane Green-Lagrange strain field is continuous at the elements' nodes.
3. For the large deformation experiment, the proposed ANCF-DIC captures the strain fields better than the Q4-DIC, particularly in the areas of strain concentrations.

4. Due to the increased number of the element's nodal parameters, the computational time of the ANCF–DIC is roughly one order of magnitude higher than that of the Q4–DIC.

The proposed image correlation procedure relates the DIC to the position-based finite-element formulation, and presents an alternative FE–DIC procedure for the study of systems undergoing finite deformation.

5. Appendix

The j -th element shape function matrix [7] is defined as

$$\mathbf{S}_j(\mathbf{x}_j) = \mathbf{S}_{ij} = \mathbf{S}_j(x_{1ij}, x_{2ij}) = \left[s_{1ij} \mathbf{I}, s_{2ij} \mathbf{I}, \dots, s_{12ij} \mathbf{I} \right], \quad (36)$$

where \mathbf{I} is 2×2 identity matrix, and

$$\begin{aligned} s_{1ij} &= -(\xi - 1)(\eta - 1)(2\eta^2 - \eta + 2\xi^2 - \xi - 1), \\ s_{2ij} &= -a\xi(\xi - 1)^2(\eta - 1), \\ s_{3ij} &= -a\eta(\eta - 1)^2(\xi - 1), \\ s_{4ij} &= \xi(2\eta^2 - \eta - 3\xi + 2\xi^2)(\eta - 1), \\ s_{5ij} &= -a\xi^2(\xi - 1)(\eta - 1), \\ s_{6ij} &= a\xi\eta(\eta - 1)^2, \\ s_{7ij} &= -\xi\eta(1 - 3\xi - 3\eta + 2\eta^2 + 2\xi^2), \\ s_{8ij} &= a\xi^2\eta(\xi - 1), \\ s_{9ij} &= a\xi\eta^2(\eta - 1), \\ s_{10ij} &= \eta(\xi - 1)(2\xi^2 - \xi - 3\eta + 2\eta^2), \\ s_{11ij} &= a\xi\eta(\xi - 1)^2, \\ s_{12ij} &= -a\eta^2(\xi - 1)(\eta - 1), \\ \xi &= x_{1ij}/a, \quad \eta = x_{2ij}/a, \end{aligned}$$

where a is the rectangular plate size.

Acknowledgments

Operation partially financed by the European Union, European Social Fund.

Table 1: Results of the simulated rigid-body translation, rigid-body rotation and deformation of a computer-generated image; ZOI corresponds to the image area without the boundary elements

	Q4-DIC			ANCF-DIC		
element size	30 × 30 pix	40 × 40 pix	50 × 50 pix	30 × 30 pix	40 × 40 pix	50 × 50 pix
ROI size	361 × 361 pix	321 × 321 pix	301 × 301 pix	361 × 361 pix	321 × 321 pix	301 × 301 pix
a)	Rigid-body translation					
	$\Delta x_1 = \bar{x}_1 - x_{01}, \Delta x_2 = \bar{x}_2 - x_{02}; x_{01} = 0.5 \text{ pix}, x_{02} = 0.5 \text{ pix}$					
Δx_1 [pix]	$-1.67 \cdot 10^{-3}$	$-4.13 \cdot 10^{-5}$	$3.65 \cdot 10^{-5}$	$-2.28 \cdot 10^{-3}$	$-2.69 \cdot 10^{-4}$	$-7.46 \cdot 10^{-5}$
Δx_2 [pix]	$1.83 \cdot 10^{-3}$	$4.95 \cdot 10^{-4}$	$2.70 \cdot 10^{-4}$	$1.32 \cdot 10^{-3}$	$-5.47 \cdot 10^{-4}$	$-5.27 \cdot 10^{-4}$
$\sigma_{\Delta x_1}$	$2.31 \cdot 10^{-2}$	$4.39 \cdot 10^{-3}$	$3.16 \cdot 10^{-3}$	$4.72 \cdot 10^{-2}$	$4.01 \cdot 10^{-2}$	$2.16 \cdot 10^{-2}$
$\sigma_{\Delta x_2}$	$2.26 \cdot 10^{-2}$	$1.12 \cdot 10^{-2}$	$4.52 \cdot 10^{-3}$	$2.33 \cdot 10^{-2}$	$6.87 \cdot 10^{-2}$	$4.21 \cdot 10^{-2}$
$\sigma_{\varepsilon_{11}}$	$8.78 \cdot 10^{-4}$	$1.00 \cdot 10^{-4}$	$6.32 \cdot 10^{-5}$	$1.23 \cdot 10^{-3}$	$7.02 \cdot 10^{-4}$	$2.39 \cdot 10^{-4}$
$\sigma_{\varepsilon_{22}}$	$6.73 \cdot 10^{-4}$	$1.41 \cdot 10^{-4}$	$5.72 \cdot 10^{-5}$	$1.50 \cdot 10^{-3}$	$7.49 \cdot 10^{-4}$	$2.52 \cdot 10^{-4}$
$\sigma_{\varepsilon_{12}}$	$5.63 \cdot 10^{-4}$	$9.86 \cdot 10^{-5}$	$4.84 \cdot 10^{-6}$	$1.19 \cdot 10^{-3}$	$9.95 \cdot 10^{-4}$	$1.66 \cdot 10^{-4}$
b)	Rigid-body rotation					
	$\Delta \varphi = \bar{\varphi} - \varphi_0, \varphi_0 = 0.017453 \text{ rad}$					
$\Delta \varphi$ [rad]	$-7.72 \cdot 10^{-4}$	$-5.13 \cdot 10^{-4}$	$-4.56 \cdot 10^{-4}$	$2.61 \cdot 10^{-3}$	$-6.79 \cdot 10^{-4}$	$-5.75 \cdot 10^{-4}$
σ_{φ}	$4.04 \cdot 10^{-3}$	$6.34 \cdot 10^{-4}$	$7.47 \cdot 10^{-4}$	$1.29 \cdot 10^{-2}$	$4.07 \cdot 10^{-3}$	$3.16 \cdot 10^{-3}$
$\sigma_{\varepsilon_{11}}$	$4.42 \cdot 10^{-3}$	$1.33 \cdot 10^{-3}$	$7.44 \cdot 10^{-4}$	$1.07 \cdot 10^{-2}$	$2.33 \cdot 10^{-3}$	$1.86 \cdot 10^{-3}$
$\sigma_{\varepsilon_{22}}$	$2.14 \cdot 10^{-3}$	$1.29 \cdot 10^{-3}$	$1.56 \cdot 10^{-3}$	$6.20 \cdot 10^{-3}$	$2.52 \cdot 10^{-3}$	$3.38 \cdot 10^{-3}$
$\sigma_{\varepsilon_{12}}$	$4.73 \cdot 10^{-3}$	$6.82 \cdot 10^{-4}$	$9.58 \cdot 10^{-4}$	$1.64 \cdot 10^{-2}$	$4.33 \cdot 10^{-3}$	$1.29 \cdot 10^{-3}$
c)	Deformation					
	$\Delta \varepsilon_{11} = \bar{\varepsilon}_{11} - \varepsilon_{011}, \Delta \varepsilon_{22} = \bar{\varepsilon}_{22} - \varepsilon_{022}, \varepsilon_{011} = 0.012, \varepsilon_{022} = 0.012$					
$\Delta \varepsilon_{11}$	$-5.45 \cdot 10^{-4}$	$-4.19 \cdot 10^{-4}$	$-3.99 \cdot 10^{-4}$	$-5.50 \cdot 10^{-4}$	$-4.65 \cdot 10^{-4}$	$-4.39 \cdot 10^{-4}$
$\Delta \varepsilon_{22}$	$-7.64 \cdot 10^{-4}$	$-5.74 \cdot 10^{-4}$	$-6.00 \cdot 10^{-4}$	$-7.63 \cdot 10^{-4}$	$-7.52 \cdot 10^{-4}$	$-5.95 \cdot 10^{-4}$
$\sigma_{\varepsilon_{11}}$	$2.25 \cdot 10^{-3}$	$1.02 \cdot 10^{-3}$	$8.16 \cdot 10^{-4}$	$9.95 \cdot 10^{-3}$	$3.03 \cdot 10^{-3}$	$1.05 \cdot 10^{-3}$
$\sigma_{\varepsilon_{22}}$	$3.76 \cdot 10^{-3}$	$1.85 \cdot 10^{-3}$	$7.99 \cdot 10^{-4}$	$5.47 \cdot 10^{-3}$	$2.72 \cdot 10^{-3}$	$1.47 \cdot 10^{-3}$
$\sigma_{\varepsilon_{12}}$	$2.00 \cdot 10^{-3}$	$9.04 \cdot 10^{-4}$	$3.54 \cdot 10^{-4}$	$1.07 \cdot 10^{-2}$	$5.12 \cdot 10^{-3}$	$9.69 \cdot 10^{-4}$

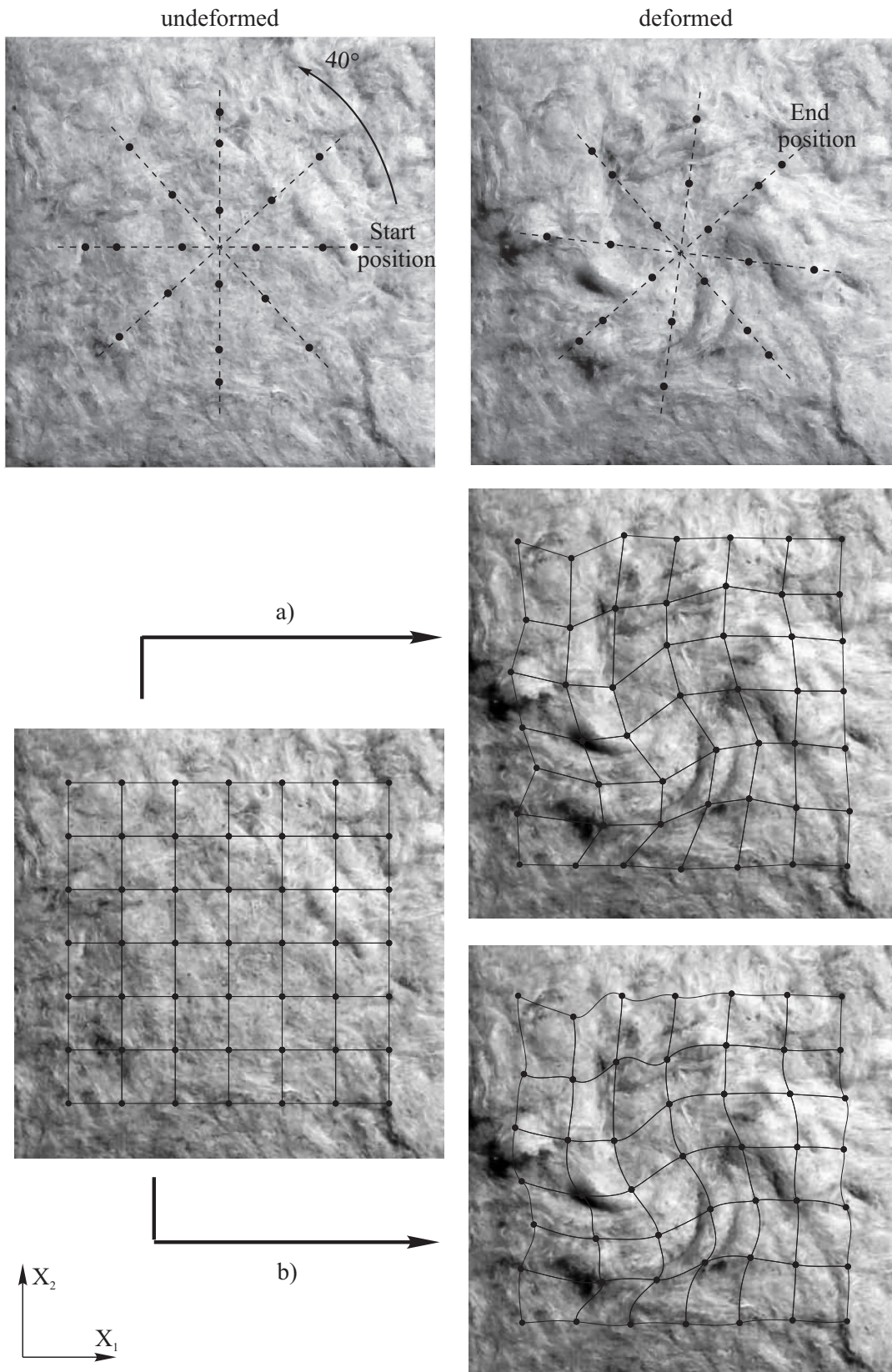


Figure 6: Comparison of the displacement fields for the a) Q4-DIC and b) the ANCF-DIC; the boundary elements are suppressed

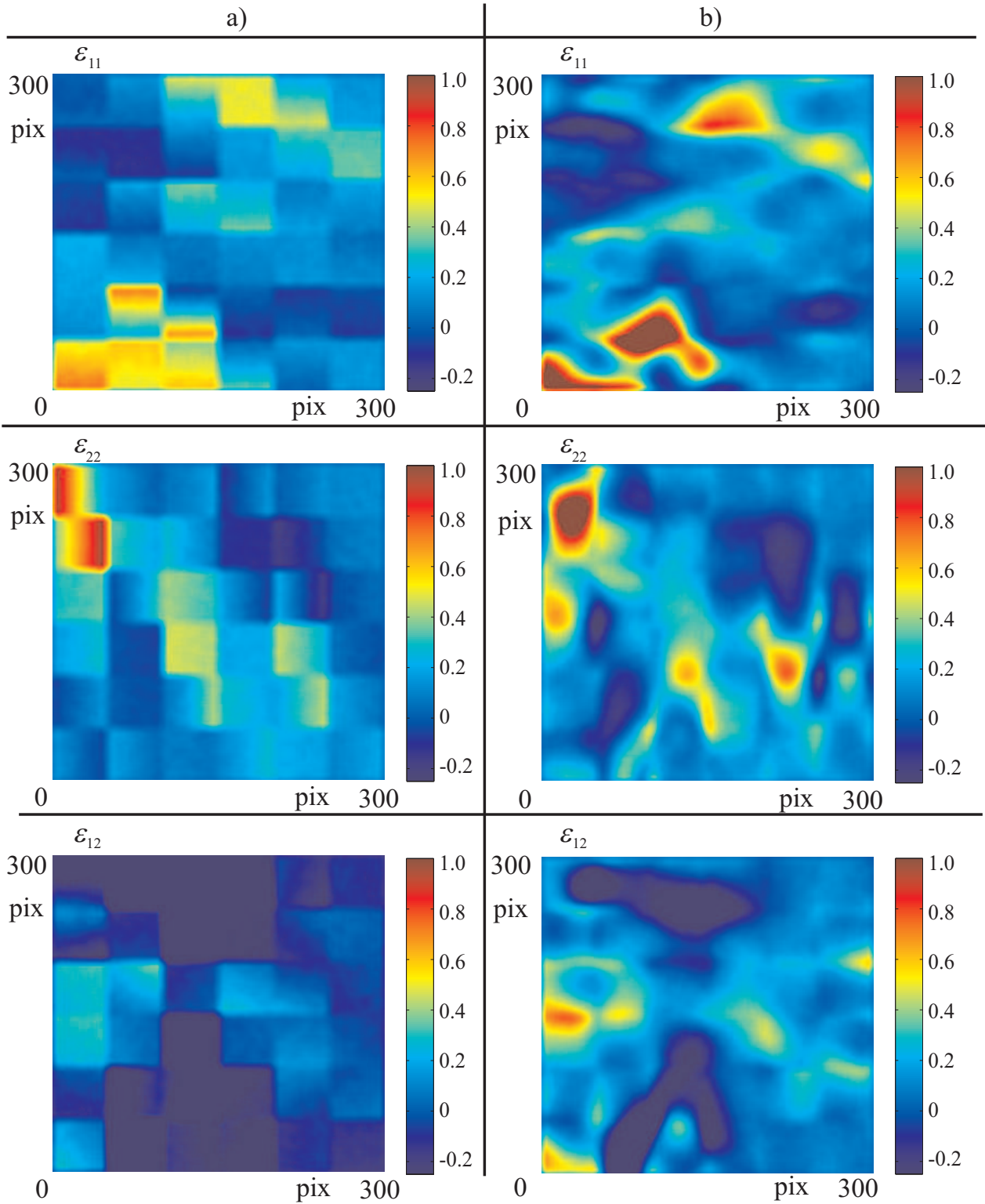


Figure 7: Comparison of the post-processed strain fields for the a) Q4-DIC and b) the ANCF-DIC

References

- [1] Avril, S., Bonnet, M., Bretelle, A., Grédiac, M., Hild, F., Ienny, P., Latourte, F., Lemosse, D., Pagano, S., Pagnacco, E., Pierron, F.: Overview of identification methods of mechanical parameters based on full-field measurements. *Experimental Mechanics* **48**, 381–402 (2008)
- [2] Besnard, G., Hild, F., Roux, S.: Finite-element displacement fields analysis from digital images: Application to portevin - le chatelier bands. *Experimental Mechanics* **46**, 789–803 (2006)
- [3] Bing, P., Hui-min, X., Bo-qin, X., Fu-long, D.: Performance of sub-pixel registration algorithms in digital image correlation. *Measurement Science and Technology* **42**, 1615–1621 (2006)
- [4] Shabana, A.: *Computational Continuum Mechanics*. Cambridge University Press (2008)
- [5] Cheng, P., Sutton, M., Schreier, H., McNeill, S.: Full-field speckle pattern image correlation with B-spline deformation function. *Experimental Mechanics* **42**, 344–352 (2002)
- [6] Dmitrochenko, O., Pogorelov, D.: Generalization of plate finite elements for absolute nodal coordinate formulation. *Multibody System Dynamics* **10**, 17–43 (2003)
- [7] Dufva, K., Shabana, A.: Analysis of thin plate structures using the absolute nodal coordinate formulation. *Proceedings of the Institution of Mechanical Engineers, Part K: Journal of Multi-body Dynamics* **219**, 345–355 (2005)
- [8] Elguedj, T., Rethore, J., Buteri, A.: Isogeometric analysis for strain field measurements. *Computer Methods in Applied Mechanics and Engineering* **200**(1-4), 40–56 (2011)
- [9] Gonzales, R., Woods, R., Eddins, S.: *Digital image processing using Matlab, 2nd edition*. Gatesmark publishing (2009)
- [10] Guo, B., Giraudeau, G., Pierron, F., Avril, S.: Viscoelastic material properties' identification using full field measurements on vibrating plates. p. 737565. SPIE (2008)
- [11] Hild, F., Roux, S.: Digital image mechanical identification (DIMI). *Experimental Mechanics* **48**(4), 495–508 (2007)
- [12] Pan, B., Qian, K., Xie, H., Asundi, A.: Two-dimensional digital image correlation for in-plane displacement and strain measurement: a review. *Measurement Science and Technology* **20**(6), 062,001 (2009)
- [13] Perie, J., Leclerc, H., Roux, S., Hild, F.: Digital image correlation and biaxial test on composite material for anisotropic damage law identification. *International Journal of Solids and Structures* **46**(11-12), 2388–2396 (2009)
- [14] Rethore, J., Elguedj, T., Simon, P., Coret, M.: On the use of NURBS functions for displacement derivatives measurement by digital image correlation. *Experimental Mechanics* **50**, 1099–1116 (2010)

- [15] Sereshk, V., Salimi, M.: Comparison of finite element method based on nodal displacement and absolute nodal coordinate formulation (ANCF) in thin shell analysis. *International Journal for Numerical Methods in Biomedical Engineering* **27**(8), 1185–1198 (2011)
- [16] Shabana, A.: Definition of the slopes and the finite element absolute nodal coordinate formulation. *Multibody System Dynamics* **1**, 339–348 (1997)
- [17] Shabana, A.: Computer implementation of the absolute nodal coordinate formulation for flexible multibody dynamics. *Nonlinear Dynamics* **16**, 293–306 (1998)
- [18] Shabana, A., Maqueda, L.: Slope discontinuities in the finite element absolute nodal coordinate formulation: gradient deficient elements. *Multibody System Dynamics* **20**, 239–249 (2008)
- [19] Shabana, A., Mikkola, A.: On the use of the degenerate plate and the absolute nodal co-ordinate formulations in multibody system applications. *Journal of Sound and Vibration* **259**(2), 481–489 (2003)
- [20] Sun, Y., Pang, J., Wong, C., Su, F.: Finite element formulation for a digital image correlation method. *Applied Optics* **44**(34), 7357–7363 (2005)
- [21] Tarigopula, V., Hopperstad, O., Langseth, M., Clausen, A., Hild, F., Lademo, O., Eriksson, M.: A study of large plastic deformations in dual phase steel using digital image correlation and FE analysis. *Experimental Mechanics* **48**, 181–196 (2008)
- [22] Čepon, G., Boltežar, M.: Dynamics of a belt-drive system using a linear complementarity problem for the belt-pulley contact description. *Journal of Sound and Vibration* **319**(3-5), 1019–1035 (2009)
- [23] Čepon, G., Boltežar, M.: Introduction of damping into the flexible multibody belt-drive model: A numerical and experimental investigation. *Journal of Sound and Vibration* **324**(1-2), 283–296 (2009)
- [24] Vendroux, G., Knauss, W.: Submicron deformation field measurements: Part 2. Improved digital image correlation. *Experimental Mechanics* **38**, 86–92 (1998)
- [25] Witz, J., Hild, F., Roux, S., Rieunier, J.: Mechanical properties of crimped mineral wools: Identification from digital image correlation. In: *IUTAM Symposium on Mechanical Properties of Cellular Materials, IUTAM Bookseries*, vol. 12, pp. 135–147 (2009)
- [26] Yu, L., Zhao, Z., Tang, J., Ren, G.: Integration of absolute nodal elements into multibody system. *Nonlinear Dynamics* **62**, 931–943 (2010)
- [27] Zhang, J., Cai, Y., Ye, W., Yu, T.: On the use of the digital image correlation method for heterogeneous deformation measurement of porous solids. *Optics and Lasers in Engineering* **49**(2), 200–209 (2011)
- [28] Zhu, Z., Pour, B.: A nodal position finite element method for plane elastic problems. *Finite Elements in Analysis and Design* **47**(2), 73–77 (2011)

- [29] Zienkiewicz, O., Taylor, R.: *Finite Element Method (5th Edition) Volume 1 - The Basis*. Elsevier (2000)
- [30] Ma, S., Zhao, Z., Wang, X.: Mesh-based digital image correlation method using higher order isoparametric elements. *Journal of Strain Analysis for Engineering Design* **47**, 163–175 (2012)
- [31] Hild, F., Roux, S., Gras, R., Guerrero, N., Eugenia, M., Flórez-López, J.: Displacement measurement technique for beam kinematics. *Optics and Lasers in Engineering* **47**, 495–503 (2009)
- [32] Hild, F., Raka, B., Baudequin, M., Roux, S., Cantelaube, F.: Multi-scale displacement field measurements of compressed mineral wool samples by digital image correlation. *Applied Optics* **41**, 6815–6828 (2002)
- [33] Langerholc, M., Česnik, M., Slavič, J., Boltežar, M.: Experimental validation of a complex, large-scale, rigid-body mechanism. *Engineering Structures* **36**, 220–227 (2012)